Graphical Abstract

A concurrent fibre orientation and topology optimisation framework for 3D-printed carbon fibre-reinforced composites

José Humberto S. Almeida Jr.,Bruno G. Christoff,Volnei Tita,Luc St-Pierre

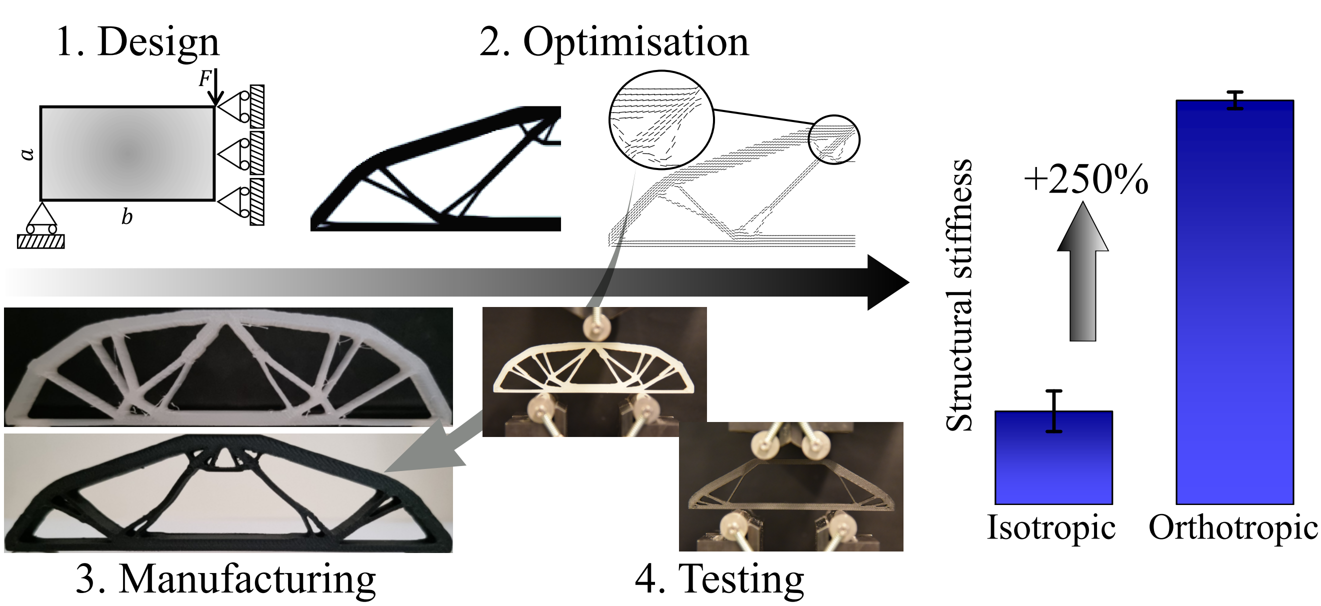

A concurrent fibre orientation and topology optimisation framework for 3D-printed carbon fibre-reinforced composites

José Humberto S. Almeida Jr.[a,b,*], Bruno G. Christoff[c], Volnei Tita[c,d] and Luc St-Pierre[b]

[a] School of Mechanical and Aerospace Engineering, Queen's University Belfast, Belfast, UK
[b] Department of Mechanical Engineering, Aalto University, Espoo, Finland
[c] Department of Aeronautical Engineering, São Carlos School of Engineering, University of São Paulo, São Carlos, SP, Brazil
[d] Department of Mechanical Engineering, Faculty of Engineering of the University of Porto, Porto, Portugal

ARTICLE INFO

Keywords:
Topology optimisation
Material optimisation
Concurrent optimisation
Additive manufacturing

ABSTRACT

This work proposes a novel framework able to optimise both topology and fibre angle concomitantly to maximise the stiffness of a structure. Two different materials are considered, one with isotropic properties (nylon) and another one with orthotropic properties (onyx, which is nylon reinforced with chopped carbon fibres). The framework optimises, in the same particular sub–step, first the topology, and second, the fibre angle at every element throughout the design domain. For the isotropic material, only topology optimisation takes place, whereas for the orthotropic solid, both topology and fibre orientation are considered. The objective function is to minimise compliance and three admissible volumes: 30%, 40%, and 50%. Three classical benchmark cases are considered: a cantilever beam, as well as 3-point and 4-point bending. The optimum topologies are further treated and manufactured using the fused filament fabrication (FFF) 3D printing method. Key results reveal that the absolute stiffness, density–normalised and volume–normalised stiffness values within each admissible volume are higher for onyx than for nylon, which proves the efficiency of the proposed concurrent optimisation framework. Moreover, although the objective function was to minimise compliance, it was also effective to improve the strength of all parts. The excellent quality and geometric tolerance of the 3D printed parts are also worth mentioning.

Highlights

- A topology optimisation framework for isotropic and orthotropic materials.
- Consideration of fibre orientation into the optimisation framework.
- Additive manufacturing of chopped carbon fibre reinforced nylon composites.
- Experimental validation: manufacturing and testing.

1. Introduction

One of the most fundamental engineering challenge is how to design a structure to be as light as possible without sacrificing its mechanical performances. According to Sigmund and Maute [1], this can be achieved with topology optimisation (TO). Its basic idea relies on repeated analysis and design update steps usually guided by a gradient-based computation. The first attempt on TO was carried out by Bendsøe and Kikuchi [2] with the aim to propose an alternative method to shape optimisation approachable to yield both the optimum topology and the optimal shape of a structure. Later on, Bendsøe [3] introduced several ways of removing the discrete nature of the problem by introducing a density function as a continuous design variable within the optimisation problem. In fact, Bendsøe and Kikuchi [2], Bendsøe [3] and Rozvany et al. [4] proposed the most disseminated mathematical approach for TO, the well-known Solid Isotropic Material with Penalisation (SIMP) method [5]. This method finds the optimal material distribution within a particular design domain, load cases, boundary conditions, manufacturing constraints, and performance requirements [6, 7]. Other less explored approaches include, for instance, the level set [8], evolutionary structural optimisation [9], and moving morphable component methods [10].

In the last 30 years, several TO approaches have been explored, mostly for isotropic materials [11]. This is mainly due to two reasons: i) the high maturity level of approaches for isotropic materials (such as SIMP) and ii) well-established manufacturing techniques for complex metallic shapes. However, the continuous demand for lightweight structures has led to the increase use of anisotropic carbon fibre-reinforced polymer (CFRP) composites, especially in high-performance aerospace, aeronautical, and automotive components [12]. From the manufacturing point of view, complex CFRP shapes can now be produced by additive manufacturing (AM) techniques [13, 14]. Among them, fused deposition modelling (FDM), or fused filament fabrication (FFF), is one of the most disseminated AM techniques, in which a polymer filament, often reinforced with fibres, is extruded and deposited on a build plate [15, 16, 17].

*Corresponding Author
humberto.almeida@qub.ac.uk (J.H.S. Almeida Jr.); brunogch@gmail.com (B.G. Christoff); voltita@sc.usp.br (V. Tita); luc.st-pierre@aalto.fi (L. St-Pierre)
ORCID(s): 0000-0002-9408-7674 (J.H.S. Almeida Jr.); 0000-0003-2148-4596 (B.G. Christoff); 0000-0002-8199-1162 (V. Tita); 0000-0003-3857-5398 (L. St-Pierre)

According to the systematic review of Sanei and Popescu [18], most studies on FFF for CFRP parts were published in the last five years only [19]. For instance, Chen and Ye [20, 21] 3D printed composite parts with carbon fibre and nylon materials using topology optimisation relying on the classical SIMP method [20] and to 3D print structures with negative Poisson's ratio [21]. Sugiyama et al. [22] 3D printed optimised composites with carbon fibres placed along the principal stress directions.

However, there is still an open question: how to arrange the reinforcing fibres and optimise the part topology? Aiming at taking full advantage of both material anisotropy and exploiting the powerful manufacturing capability of FFF method, an adequate answer is by combining TO to optimise the material distribution with structural optimisation to adjust the local fibre orientation. On the one hand, the material distribution can be optimised using SIMP; on the other hand, the fibre angle can be locally optimised with gradient-based algorithms, in which the fibre angle can be treated as a design variable [23].

There are a few studies dealing with both topology and fibre angle optimisations simultaneously. For example, Lee et al. [24] developed a TO method for optimising both material layout and fiber orientation in functionally graded fiber-reinforced composites, in which the fibre angle are considered as discrete variables. Tong et al. [25] built a sequential optimisation method considering both fibre angle and topology for constant-stiffness laminated plates using lamination parameters as design variables. The stiffness for a short cantilever beam and the flexibility for a compliant inverter increased by 6.5% and 4.2%, respectively. Jiang et al. [26] proposed a TO approach for continuous fiber angle optimisation, which computes the best layout and orientation of fiber reinforcement for AM structures. They report a minimum compliance 63% lower than the baseline by selecting a different print orientation, in which the fiber orientation follows the outer contour of the dense material region for each layer. Nomura et al. [27] developed a TO framework for designing both topology and orientation distributions of composite materials simultaneously. However, the optimisation results have some areas which violate the conditions for tensor invariants. Papapetrou et al. [28] developed an optimisation framework for both topology and fibre paths to create variable-stiffness designs. In general, the optimised part is stiffer than the baseline. Yan et al. [29] proposed a concurrent hierarchical optimisation methodology considering the simultaneous optimisation of structural topology and orthotropic material orientation. They showed by means of numerical examples that optimising both topology and fibre angle might decrease compliance. Among these studies, only Jiang et al. [26] manufactured optimum beams using carbon-fiber-reinforced polylactic acid (PLA) composites. However, only one type of specimen and one volume was 3D-printed. Nevertheless, all the other mentioned studies are merely computational. Chen and Ye [20] developed a procedure combining topological design and fibre placement paths based on average load transmission trajectories for 3D-printed CFRP parts using the classical SIMP method for optimising the topology.

After the non–extensive state–of-the–art on research undertaken on the topic, the following gaps have been identified, which underlie the realisation of this study:

- no studies are considering the anisotropy of carbon fibres in the topology optimisation;
- there is need for a framework that can simultaneously optimise both topology and fibre angle;
- no investigations are considering chopped carbon fibre reinforced thermoplastic composites; and
- there is a lack of comprehensive investigations considering the whole design process: from optimisation to manufacturing and testing.

In this context, this work proposes a robust concurrent topology and fibre angle optimisation framework for 3D-printed composites using dedicated algorithms considering the orthotropy of the composite materials in contrast to the classical SIMP approach. The topology problem is solved as a constrained problem whereas the fibre angle is treated as an unconstrained optimisation problem. Three final volumes are selected (30%, 40%, and 50%), and the objective function is compliance minimisation. Three benchmark cases are considered to evaluate the novel approach herein developed: i) cantilever beam, ii) three-point bending, and iii) four-point bending (or MMB beam). Two materials properties are considered: isotropic and orthotropic. The isotropic material consists of nylon (Polyamide 6 – nylon), whereas the transversely isotropic material is a chopped carbon-fibre filled nylon, called onyx. After the numerical optimisation is finished, the optimal 3-point and 4-point bending beams are 3D printed, with both nylon and onyx materials, and tested under the same boundary conditions (BC) used in the optimisation.

2. The formulation

Let Ω be a domain in $\mathbb{R}^2$ with boundary $\partial\Omega$ (Figure 1). Consider that the Dirichlet and Neumann boundary conditions are applied on $\partial\Omega_u$ and $\partial\Omega_f$, respectively, where

$$\partial\Omega = \partial\Omega_{u_i} \cup \partial\Omega_{f_i}; \quad \partial\Omega_{u_i} \cap \partial\Omega_{f_i} = \emptyset \quad i = 1, 2, \tag{1}$$

such that

$$u_i = u_i^g \quad \text{on} \quad \partial\Omega_{u_i} \quad i = 1, 2, \tag{2}$$

where u_i is the i-th component of the displacement and u_i^g is known, and

$$\sigma_{ij} n_j = t_i \quad \text{on} \quad \partial\Omega_{f_i} \quad i = 1, 2, \tag{3}$$

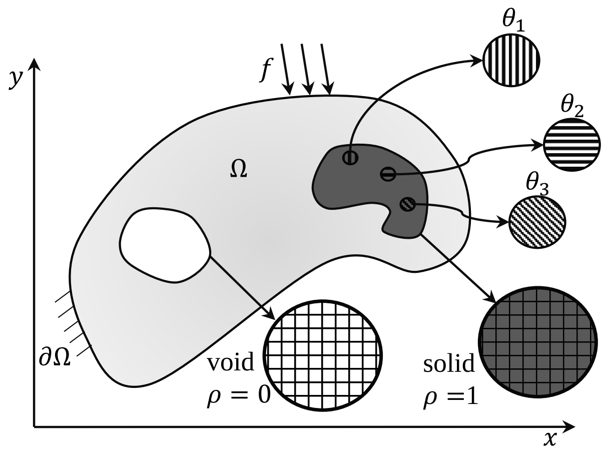

Figure 1: Schematic representation of both topology and fibre orientation within a given domain.

where $\boldsymbol{\sigma}$ is the stress tensor, $\boldsymbol{n}$ is a normal unit vector and t_i is the traction vector.

We want to find the optimal material distribution that minimises compliance when subjected to boundary conditions Eqs. (2) and (3). For this purpose, domain Ω is divided into n finite elements, such that

$$\Omega = \bigcup_{e=1}^{n} \Omega_e. \tag{4}$$

Each element e has a relative density ρ_e and an angle θ_e, which corresponds to the fibre orientation. Thus, element e has an elasticity matrix $\boldsymbol{C}_e = \boldsymbol{C}_e\left(\rho_e, \theta_e\right)$ parametrised by

$$\boldsymbol{C}_e = \rho_e^P \boldsymbol{C}_e^g, \tag{5}$$

where $\boldsymbol{C}_e^g = \boldsymbol{C}_e^g\left(\theta_e\right)$ is the elasticity matrix of the base material in a global coordinate system and $\boldsymbol{P}$ is a penalisation factor. A plane-stress consideration is adopted, and the elasticity tensor is

$$\boldsymbol{C}^l = \begin{bmatrix} C_{1111} & C_{1122} & 0 \\ C_{1122} & C_{2222} & 0 \\ 0 & 0 & C_{1212} \end{bmatrix} \tag{6}$$

in its local coordinate system and this is transformed to the global coordinate system with

$$\boldsymbol{C}_e^g = \boldsymbol{R}_e^T \boldsymbol{C}^l \boldsymbol{R}_e, \tag{7}$$

where $\boldsymbol{R}_e = \boldsymbol{R}_e\left(\theta_e\right)$ is the rotation matrix for element e.

The optimisation problem is stated as

$$\begin{aligned} \min_{\rho,\theta} \quad & f = \boldsymbol{F}^T \boldsymbol{U} \\ \text{s.t.} \quad & V \leq \bar{V} \\ & \boldsymbol{KU} = \boldsymbol{F} \\ & \rho_{min} \leq \rho_e \leq 1.0 \end{aligned} \tag{8}$$

where $f = f(\boldsymbol{\rho}, \boldsymbol{\theta})$ is the compliance of the structure, $\boldsymbol{F}$ is the vector of external forces, $\boldsymbol{U} = \boldsymbol{U}(\boldsymbol{\rho}, \boldsymbol{\theta})$ is the displacement vector, $V = V(\boldsymbol{\rho})$ is the volume of the structure, $\bar{V}$ is a fixed volume (upper bound), $\boldsymbol{K} = \boldsymbol{K}(\boldsymbol{\rho}, \boldsymbol{\theta})$ is the global stiffness matrix and ρ_{min} is the minimum value adopted for the relative density, used to avoid numerical issues during both the optimisation procedure and solving the linear system.

The optimisation problem stated in Eq. (8) can be written as an unconstrained problem using the Lagrangian function, leading to

$$\begin{aligned} \min_{\rho,\theta} \quad & L = \boldsymbol{F}^T \boldsymbol{U} + \lambda\left(V - \bar{V}\right) \\ \text{s.t.} \quad & \boldsymbol{KU} = \boldsymbol{F} \\ & \rho_{min} \leq \rho_e \leq 1.0, \end{aligned} \tag{9}$$

where $L = L(\boldsymbol{\rho}, \boldsymbol{\theta})$ is the Lagrangian function and λ is the Kuhn-Tucker multiplier. The minimum is reached when

$$\nabla_{\rho,\theta} L = \mathbf{0}. \tag{10}$$

Note that the volume constraint is dependent only on ρ (and independent of θ). Therefore, the procedure can be separated into a constrained and an unconstrained problem to be solved sequentially. Derivating Eq. (10) with respect to $\boldsymbol{\rho}$, returns

$$\nabla_\rho L = \nabla_\rho f + \lambda \nabla_\rho V = \mathbf{0}. \tag{11}$$

As shown in [30], the q-th relative density can be updated by

$$\rho_q^{k+1} = \rho_q^k \beta_q^\eta, \tag{12}$$

where η is a relaxation parameter and β_q is the update parameter, given by

$$\beta_q = \frac{\frac{df}{d\rho_q}}{\lambda \frac{dV}{d\rho_q}}. \tag{13}$$

The derivatives of the compliance and of the volume in relation to the $q-$th relative density are given by

$$\frac{df}{d\rho_q} = \boldsymbol{u}_q^T \left(\sum_{m=1}^{pg} \boldsymbol{B}_q^T \left(P \rho_q^{P-1} \right) \boldsymbol{C}_q^g \boldsymbol{B}_q W_m J_m \right) \boldsymbol{u}_q \tag{14}$$

and

$$\frac{dV}{d\rho_q} = V_q, \tag{15}$$

respectively, where $\boldsymbol{B}_q$ is the strain-displacement matrix of the q-th element of the mesh, pg is the number of Gauss points used for the numerical integration, $\boldsymbol{W}_m$ and $\boldsymbol{J}_m$ are, respectively, the quadrature weight and determinant of the Jacobian matrix associated to Gauss point m.

Now, taking the gradient from Eq. (10) with respect to $\boldsymbol{\theta}$, gives

$$\nabla_{\boldsymbol{\theta}} L = \mathbf{0} = \nabla_{\boldsymbol{\theta}} f, \tag{16}$$

which is an unconstrained problem. The derivative of the compliance with respect to the q-th angle is

$$\frac{df}{d\theta_q} = \boldsymbol{u}_q^T \left(\sum_{m=1}^{pg} \boldsymbol{B}_q^T \rho_q^P \frac{d\boldsymbol{C}_q^g}{d\theta_q} \boldsymbol{B}_q \boldsymbol{W}_m \boldsymbol{J}_m \right) \boldsymbol{u}_q \tag{17}$$

in which the derivative of the elasticity matrix with respect to θ_q can be obtained analytically from Eq. (7). The unconstrained problem is solved using the Steepest Descent method with a Golden section algorithm for the line search.

Considering that the derivatives represent a local behaviour of the function, a scheme of moving limits is adopted. These constraints are

$$\rho_q^{k+1} \in \left[\rho_q^k - d_q^1, \rho_q^k + d_q^1 \right] \tag{18}$$

for the relative density and

$$\theta_q^{k+1} \in \left[\theta_q^k - d_q^2, \theta_q^k + d_q^2 \right], \tag{19}$$

for the angle of each element, where d_q^1 and d_q^2 are positive moving limits for the q-th relative density, and the q-th angle, respectively. The moving limits change at each iteration depending on the behaviour of the design variable. If the design variable changes monotonically in three subsequent steps, the moving limit is updated by a factor higher than 1.0, and if the design variable oscillates in those steps, the moving limit is updated by a factor lower than 1.0.

In topology optimisation problems, two significant issues may occur. The first one is the appearance of patterns similar to a checkerboard, in which a region has, alternately, solid and void elements. The second one is the mesh-dependency of the results, in which different results are obtained for different mesh sizes [31]. Thus, a filtering scheme is adopted to avoid numerical instabilities in the optimisation procedure. A basic sensitivity filtering scheme [31] is used for both relative density and fibre angle. Consider a region of radius R around an element e, which is given by

$$N_e = \left\{ j, \|\boldsymbol{c}_j - \boldsymbol{c}_e\| \leq R \right\}, \tag{20}$$

where $\boldsymbol{c}_j$ and $\boldsymbol{c}_e$ are the centroid of elements j and e, respectively. The dependency of the design variable of element e on its neighbours is written as

$$\widetilde{\frac{\partial f}{\partial \rho_e}} = \frac{\sum_{j \in N_e} w\left(\boldsymbol{c}_j\right) \rho_j \frac{\partial f}{\partial \rho_j}}{\rho_e \sum_{j \in N_e} w\left(\boldsymbol{c}_j\right) v_j}, \tag{21}$$

where $w(\boldsymbol{c}_j)$ is a weighting function, chosen here as a linear decaying one.

A flowchart of the whole optimisation procedure is shown in Figure 2. All steps are performed with an in-house code written in Julia Language [32]. The data needed for the optimisation is an input to the algorithm. This includes the geometry, mesh, all the variables for the topology optimisation, material properties and boundary conditions. The last step before starting the optimisation procedure is to create two vectors $\boldsymbol{\rho}_1$ and $\boldsymbol{\theta}_1$ containing the initial estimate for both design variables. The input data used in all simulations is shown in Appendix A.

The optimisation procedure itself is performed sequentially. For each global optimisation step, the topology optimisation is performed first, followed by the material optimisation.

During the topology optimisation, the equilibrium problem for the current step n is solved for ρ_n and θ_n. Then, the derivatives of the compliance about the ρ_n are obtained with Eq. (14) and used to update the relative densities to ρ_{n+1} according to Eq. (12) while respecting the moving limits imposed in Eq. (18).

The material optimisation step is conducted with the variables ρ_{n+1} and θ_n, see Figure 2. First, the derivatives of the compliance about the fibre angles are evaluated with Eq. (17). Second, the fibre angles are updated to θ_{n+1} using the steepest descent algorithm, while respecting the moving limits imposed in Eq. (19). In both topology and material optimisation, a sensitivity filtering scheme, Eq. (21), is adopted.

Convergence is reached when the compliance, relative densities, and fibre angles have a variation inferior to 1% in ten subsequent steps. If convergence is not satisfied, one assumes $n = n + 1$, and the procedure returns to the topology optimisation. When convergence is reached, a plain text file is generated containing the compliance, a vector of relative densities and a vector of fibre angles. This format is such that the optimum geometry and fibre orientation can be visualised using the software Gmsh [33].

3. The optimisation

3.1. Study cases

The optimisation framework is tested on three design cases: cantilever, 3-point bending and 4-point bending beams, as shown in Figure 3. These are classical benchmark cases in TO, allowing us to compare our results with other

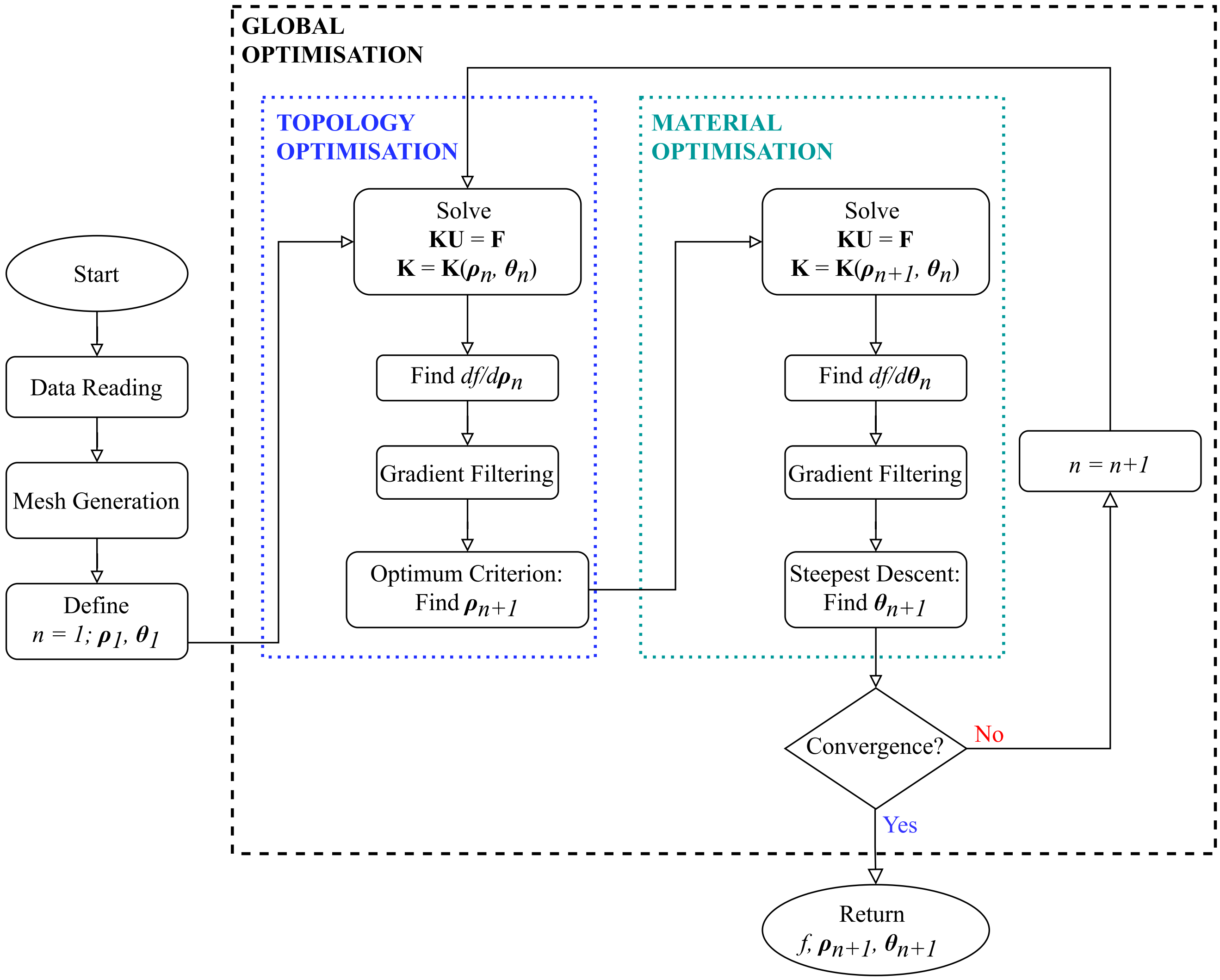

Figure 2: Flowchart of the optimisation framework.

approaches available in the literature. In all cases, the problem is 2D (plane stress) and the optimisation domain has a height $a = 30$ mm and a width $b = 60$ mm, see Figure 3. Considering that the symmetry line is located at $b = 0$, the supporting pins are located at $0.9b$ for both 3-point and 4-point bending, whereas the force on the 4-point bending case is applied at $0.1b$. The domain is discretised by 180×90 regular bi-linear isoparametric elements with incompatible modes [34]. An example of the finite element mesh, alongside the final optimisation topology, is shown in Figure 4. A filter radius $R = 0.5$ mm is used in all cases to guarantee that two adjacent elements are within the filtering radius. For each design case, the optimisation is conducted for three different final volumes: $V = 30\%$, 40%, and 50% of the initial design domain.

The optimisation is conducted with two different materials, one isotropic and one orthotropic, to quantify the effect of fibre orientation. The isotropic solid has the properties of nylon, whereas the orthotropic material, has those of onyx. These two materials are the same as those used in the experiments presented in Section 4.2. The properties of both materials are presented in Table 1. The isotropic material, nylon, is characterised by an elastic modulus $E = 0.98$ GPa and a Poisson's ratio $\nu = 0.42$.

Table 1
Experimentally measured elastic and physical properties for both nylon and onyx materials.

Nylon (n)		Onyx (o)	
E (GPa)	0.98	E_1 (GPa)	1.26
ν (–)	0.42	E_2 (GPa)	0.33
ρ (g/cm^3)	1.1	G_{12} (GPa)	0.37
G (GPa)	0.35	ν_{12} (–)	0.39
		ρ (g/cm^3)	1.18

On the other hand, Onyx is a composite material in which nylon is reinforced with chopped carbon fibres. Onyx comes as a filament (to be used in fused filament fabrication) where the chopped fibres are predominantly aligned with the filament direction, which leads to an orthotropic behaviour. The

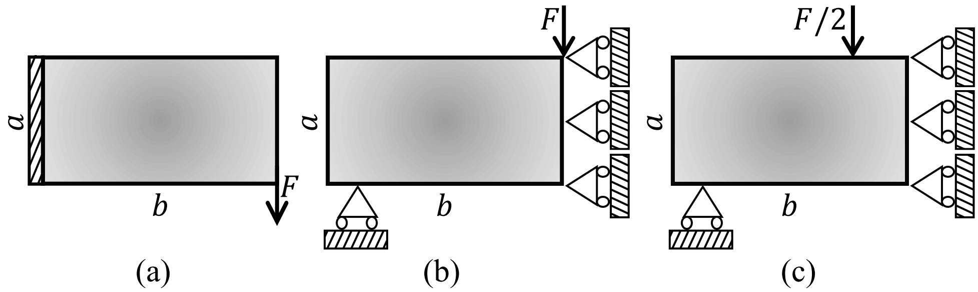

Figure 3: Design domain, loads, and boundary conditions for (a) cantilever, (b) 3-point bending, and (c) 4-point bending cases.

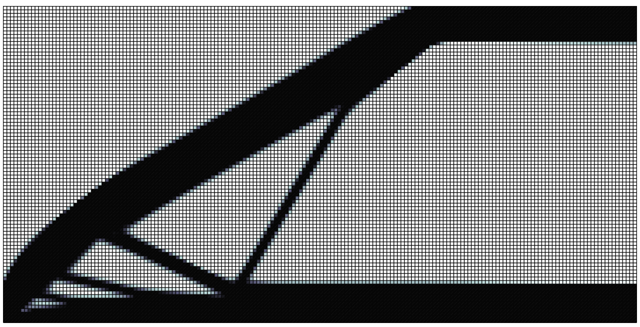

Figure 4: The convergence–free finite element mesh used in all optimisation cases.

Onyx filaments have a fibre volume fraction $V_f \approx 15\%$, and the carbon fibres have an average diameter $\phi_f = 6$ µm and length $l_f = 100$ µm.

Uniaxial tests have been performed in both Onyx and Nylon materials to characterise their elastic moduli, E_1 for onyx and E for nylon, and the Poisson's ratio, ν, for nylon. Those values are given in Table 1. With these characteristics, it is possible to derive the other properties for the orthotropic material using the Halpin–Tsai model for short fibre-reinforced composites [35]. The transverse elastic modulus E_2 is given by:

$$E_2 = E_m\left(\frac{1+\zeta\eta_2 V_f}{1-\eta_2 V_f}\right); \eta_2 = \frac{\left(\frac{E_{1,f}}{E_m}\right)-1}{\left(\frac{E_{1,f}}{E_m}\right)+\zeta}; \zeta = 2 \quad (22)$$

where the elastic moduli of the fibres $E_{1,f} = 230\,\mathrm{GPa}$ and of the matrix $E_m = 0.98\,\mathrm{GPa}$. Otherwise, the in-plane shear modulus G_{12} is given by:

$$G_{12} = G_m\left(\frac{1+\zeta\eta_3 V_f}{1-\eta_3 V_f}\right); \eta_3 = \frac{\left(\frac{G_{12,f}}{G_m}\right)-1}{\left(\frac{G_{12,f}}{G_m}\right)+2}; \zeta = 1 \quad (23)$$

where the shear moduli of the fibres $G_{12,f} = 104.5\,\mathrm{GPa}$ ($G_{12,f} = E_{1,f}/2(1+\nu_{12,f})$) and of the matrix $G_m = 0.35\,\mathrm{GPa}$ ($G_m = E_m/2(1+\nu_m)$). Finally, the major Poisson's ratio is given by:

$$\nu_{12} = \nu_{12,f}V_f + \nu_m V_m; \nu_{12} = \nu_{21}\frac{E_2}{E_1} \quad (24)$$

where the Poisson's ratio of the fibres $\nu_{12,f} = 0.1$ and that of the matrix is $\nu_m = 0.42$. The orthotropic properties of onyx are included in Table 1 whereas an overview of all design cases considered is provided in Table 2.

Table 2
Nomenclature for the specimens and their parameters.

Case	V (ρ)	R (mm)	Material
cb_30_n	30%	0.5	Nylon
cb_30_o			Onyx
3pb_30_n			Nylon
3pb_30_o			Onyx
4pb_30_n			Nylon
4pb_30_o			Onyx
cb_40_n	40%	0.5	Nylon
cb_40_o			Onyx
3pb_40_n			Nylon
3pb_40_o			Onyx
4pb_40_n			Nylon
4pb_40_o			Onyx
cb_50_n	50%	0.5	Nylon
cb_50_o			Onyx
3pb_50_n			Nylon
3pb_50_o			Onyx
4pb_50_n			Nylon
4pb_50_o			Onyx

3.2. Optimisation results

A convergence analysis of the objective function is shown in Figure 5 for the 3pb_30_n optimisation case. In this case, the compliance is calculated at the end of each global step of the optimisation procedure, meaning that both topology and material optimisations are performed to obtain the value of the objective function. All optimisation cases follow the same convergence behaviour, therefore only one plot is presented as it is representative of all cases.

As stated earlier, convergence is reached when the objective function and the design variables do not vary by more than 1% in ten subsequent global steps. Furthermore, the

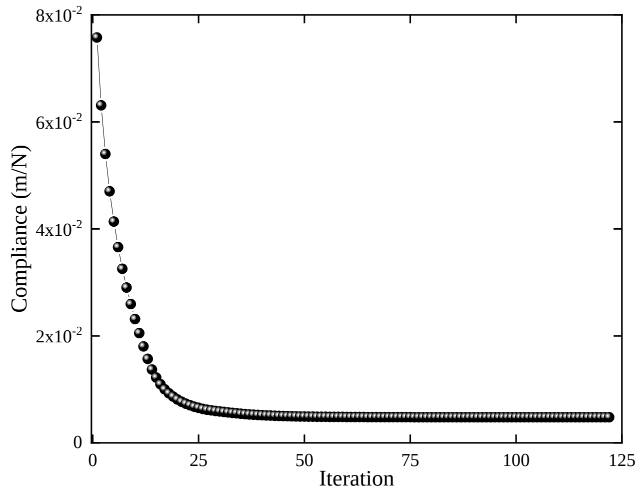

Figure 5: Convergence plot for the 3pb_30_n case.

convergence is monotonic, which shows the consistency of the implemented algorithm. Finally, for both isotropic and orthotropic cases, the objective function behaves akin to the convergence analysis shown in Figure 5.

The optimal topologies for isotropic and orthotropic materials are compared in Figure 6. The results show that the topologies for the isotropic and orthotropic materials differ from each other; there are differences in the reinforcements, especially for $V = 0.3$. The nature of the materials themselves makes it reasonable to expect such differences. In the orthotropic case, the fibres have a preferential stiffness direction, and the direction of the fibres is optimised alongside the topology. In this case, the topology optimisation step influences the material optimisation step and vice-versa. Those features are not present in the isotropic case. Moreover, when the same case with different volume fractions is considered, one can notice a pattern in the topologies. Basically, the higher the admissible volume of the structure, the bigger the reinforcements and the larger the number of reinforcements. Thus, the implemented algorithms show consistency.

In addition, Figure 7 shows the optimal fibre distribution for the orthotropic cases. The fibre angles follow the reinforcements, which can be seen in details in the highlighted areas. This was expected since the fibres oriented in the span direction provide a higher stiffness to the structure, thus reducing its compliance.

4. Experimental details

The optimal 3-point and 4-point bending beams were manufactured and tested to verify the efficiency of the optimisation algorithm. The cantilever beam was excluded from these tests as it is difficult to achieve perfectly clamped boundary conditions in experiments. This section details the approach followed to convert the TO output into an STL file, as well as the 3D printing and testing procedures.

4.1. The STL file generation

Most rapid prototyping techniques and 3D printers require the geometry to be provided as an STL file [36]. Therefore, we have to convert the output from TO into a three-dimensional STL file. This is done using three different tools as depicted on the flowchart in Figure 8. First, a rough STL file is created using an in-house algorithm. Second, the STL mesh is verified and smoothed using MeshLab. Third, Blender is used to correct minor issues with the mesh, if necessary. The entire procedure is detailed below.

The first step is performed with an in-house algorithm written in Julia Language [32]. The input for the algorithm is a plain text containing the connectivity of each element of the FE mesh and its relative density. The optimisation was done on a 2D plane stress model and using symmetric boundary conditions (see Section 3); therefore, our algorithm uses extrusion and mirroring to generate the full 3D geometry. The optimisation process often produces elements with intermediate relative densities ($0 < \rho_e < 1$), which cannot be part of the final geometry. Our algorithm uses a threshold value ρ_t such that elements with relative densities above the threshold are assumed as solid and those below ρ_t are considered voids (see Figure 1). In all cases, ρ_t is selected such that the admissible volume is maintained. Afterwards, the algorithm generates a crude STL file from optimisation data. For each face of every element on the FE mesh, a triangle of coordinates is generated alongside a normal vector. All triangles follow the right-hand rule and their normals point outward.

Next, we use the mesh processing software MeshLab [37] to verify and improve the STL model. The STL file created in the first step contains duplicate faces and vertices for adjacent elements, and we use MeshLab to remove these duplicate features. Then, the mesh quality is verified to ensure that it is 'watertight', free of holes/gaps, and does not contain any intersecting/overlapping triangles [38]. If any problems are detected, then the mesh is corrected manually, and this is done is two steps. First, the mesh is simplified to a two-dimensional geometry by deleting elements in the out-of-plane direction. Second, the 2D mesh is exported and opened with the software Blender [39], which includes built-in tools for repairing STL meshes. The main issue encountered in this work consisted of elements connected by a single vertex as shown in Figure 8. After correcting the issues, the geometry is extruded into a 3D part and re-opened in MeshLab to verify the mesh quality.

Once the quality of the mesh is satisfactory, the last step is to smooth the geometry to eliminate the pixelated contours caused by the optimisation procedure. This is done with the Laplacian smoothing method, where the position of each vertex is adjusted based on the weighted positions its neighbours [40]. Finally, a new STL file is generated containing the quality-checked, smoothed mesh. Then, the fibre orientation of each element is translated to the 3D printer afterwards.

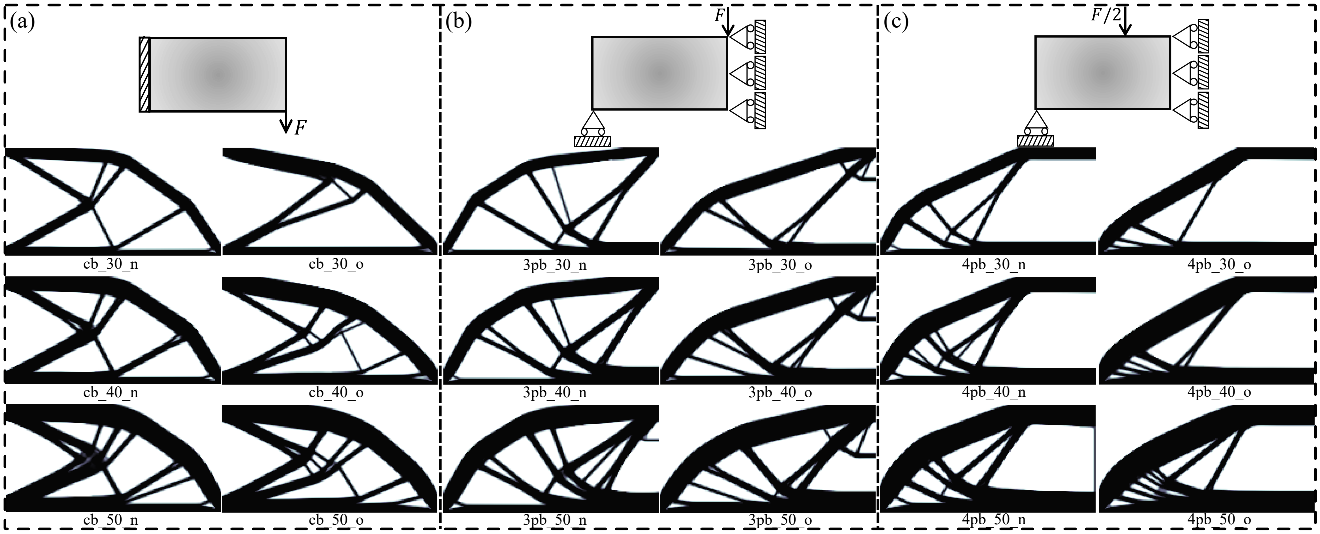

Figure 6: Optimal topologies for (a) cantilever, (b) 3-point bending, and (c) 4-point bending beams.

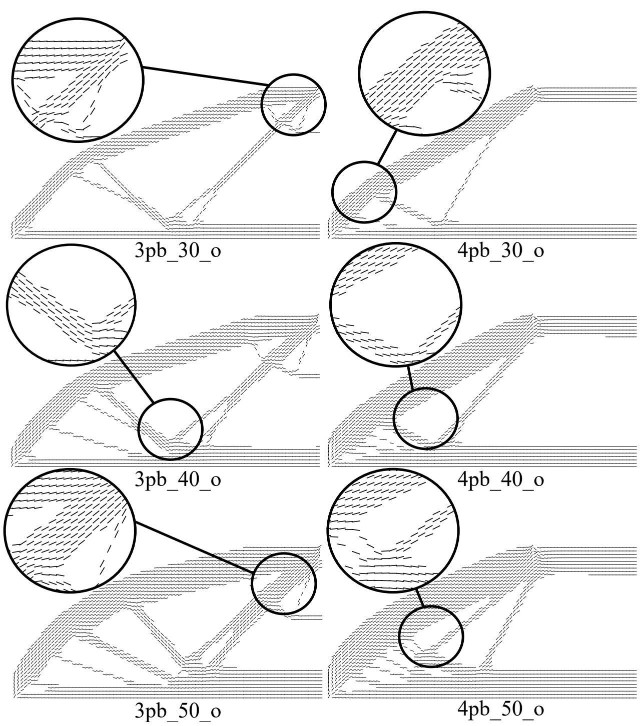

Figure 7: Optimal fibre angle for the optimised (a) 3-point bending and (b) 4-point bending beams.

4.2. Additive manufacturing & testing

All samples were printed using a Mark Two 3D printer (Markforged Inc., USA), which uses fused filament fabrication. Both printing materials (nylon and onyx) were stored in a dry storage box to limit moisture retention prior to printing. The filaments were heated within the printer's head and laid layer-by-layer, consolidating under atmospheric conditions. From each simulation, the .stl files were sliced using the Markforged cloud-based software, Eiger [41]. A layer height of 0.1 mm and solid infill were selected to provide as accurate detail as possible. All parts had the same overall dimensions: $120 \times 30 \times 8\,\text{mm}^3$, and were made up of 80 layers.

All samples were tested in 3-point and 4-point bending. The tests were carried out with a displacement rate of 2 mm/min in a MTS universal testing machine equipped with a load cell of 30 kN. A span-to-thickness ratio of 16:1 was used, based on the recommendations of ASTM D7264 standard.

4.3. Experimental results

The experimental load versus displacement curves for all nylon and onyx topologies under 3-point bending are shown in Figure 9 (graphs with different axis limits for better visualisation of results and curve shapes). All samples have a fairly ductile response, which is beneficial for composite structural components since their inherent brittleness is perhaps the main bottleneck that prevents their use in primary structures. As expected, the stiffness and strength increase with increasing volume. This holds true for both materials. Another remarkable characteristic is the excellent repeatability: each test was repeated five times and the standard deviation is very low for both stiffness and strength. Focusing on the effect of the parent material, we observe the following:

3-point bending:

- Nylon (Figure 9(a,c,e)): regardless of the volume, the curves have a similar shape, with a linear–elastic increase up to a peak force, followed by a gradual softening due to plastic deformation. Increasing the final volume increases the deflection at peak force, which is mainly due to an increase in structural stiffness and strength.
- Onyx (Figure 9(b,d,f)): in general, the responses are similar, but different from those of nylon sam-

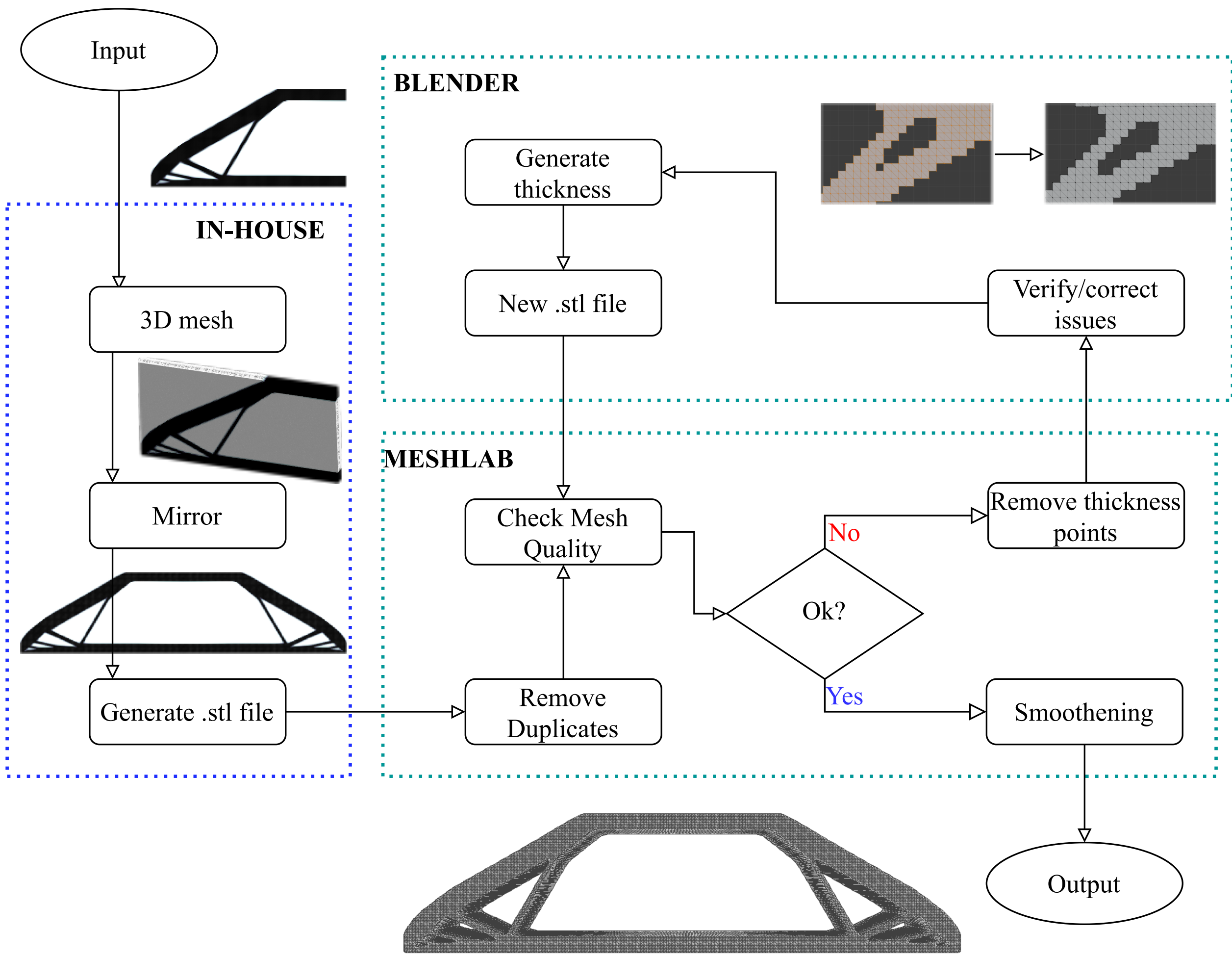

Figure 8: Flowchart of the procedure to transform the output from optimisation into a printable STL file.

ples. Firstly, these samples are significantly stiffer and stronger than the nylon ones, which was expected since they have reinforcing fibres. Nevertheless, even though the reinforcing fibres are as small as 100 μm, they have a strong effect on the structural response of the parts thanks to the great efficiency of the concurrent optimisation framework herein developed. Secondly, onyx samples exhibit a sharp load drop after the peak force, followed later by a gradual softening. No full loss of structural response is observed for any parts, which is attractive for structural components since the part can still carry load after cracking and/or elastic buckling occur.

4-point bending:

- Nylon (Figure 10(a,c,e)): all responses are similar to those measured under 3-point bending; there is a linear-elastic regime up to a peak load. Nonetheless, the post-peak plastic deformation is slightly different and occurs at a roughly constant load level. This is attributed to the better load distribution onto the compressive side of the sample.
- Onyx (Figure 10(b,d,f)): again, these specimens are significantly stiffer and stronger than nylon samples. Similarly to nylon specimens, onyx samples display very little or no post-peak softening under 4-point bending.

5. Discussion

The final deformed shapes, after unloading, for all parts are shown in Figure 11. There are no fractured trusses observed on any specimens. For nylon samples, plastic deformation and local buckling are the most dominant failure mechanisms. Otherwise, minor cracking and elastic buckling are the main failure mechanisms for onyx specimens. Onyx parts also have more pronounced out-of-plane deformation and intralaminar fracture on the compressive side of the specimens (upper edge) when compared to nylon samples. It is worth mentioning that interlaminar failure (delamination) was not observed in any specimens. We anticipate that delamination would be more prevalent if the polymer was reinforced with continuous fibres, in-line with the observations of Chen and Ye [20].

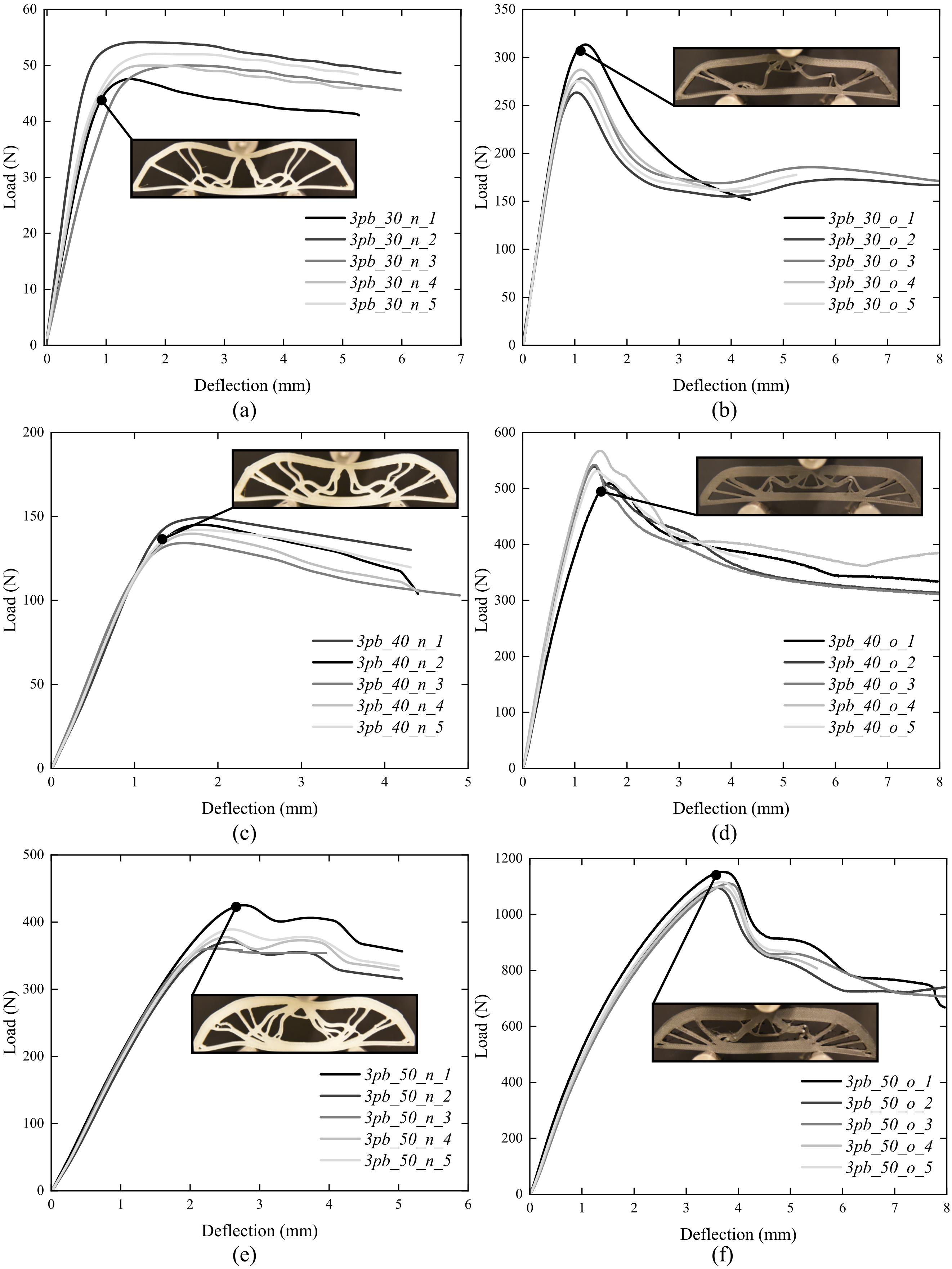

Figure 9: Experimental load-deflection curves for 3-point bending beams: (a) 3pb_30_n, (b) 3pb_30_o, (c) 3pb_40_n, (d) 3pb_40_o, (e) 3pb_50_n, (f) 3pb_50_o. A representative photograph of the part taken at the peak load is shown for each group. *Graphs with different axes limits for better visualisation of the curves.*

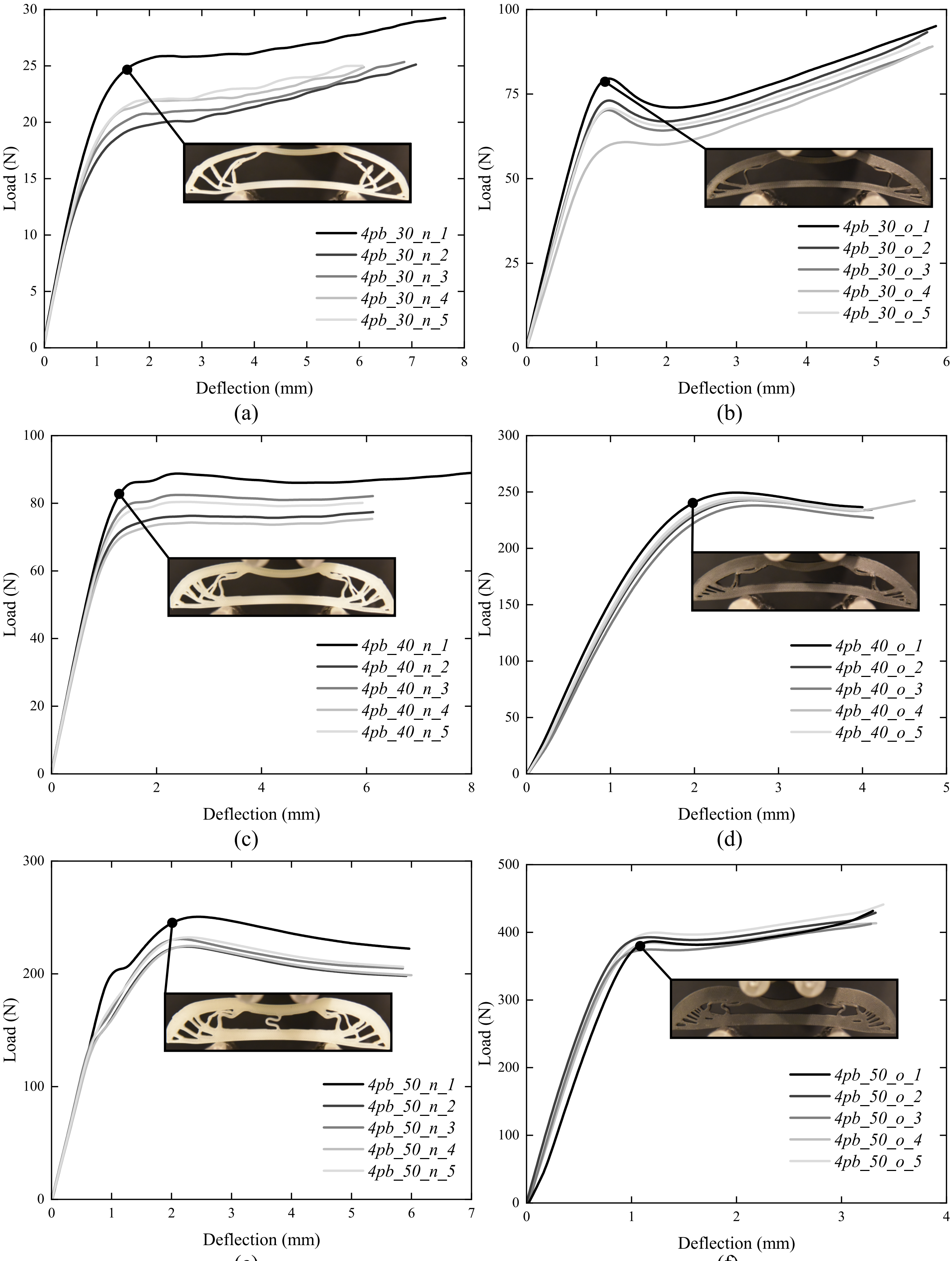

Figure 10: Experimental load-deflection curves for 4-point bending beams: (a) 4pb_30_n, (b) 4pb_30_o, (c) 4pb_40_n, (d) 4pb_40_o, (e) 4pb_50_n, (f) 4pb_50_o. A representative photograph of the part taken at the peak load is shown for each group. *Graphs with different axes limits for better visualisation of the curves.*

Figure 11: Deformed shapes for all 3D printed parts after unloading.

The structural stiffness K is given in Figures 12(a) and 12(d) for 3-point and 4-point bending tests, respectively. As expected, increasing the admissible volume increases the structural stiffness. In addition, the structural stiffness of Onyx specimens is considerably higher than that of nylon samples. This is surprising considering that the properties of nylon are between the bounds of the onyx properties, i.e., $E_2 < E < E_1$, see Table 1. This improvement in structural stiffness shows the efficiency and purpose of the present framework.

The density-normalised stiffness is shown in Figure 12(b,e), whereas the volume-normalised stiffness is given in Figure 12(c,f). Both the density- and volume-normalised stiffnesses confirm that onyx samples are significantly stiffer than their nylon counterparts.

6. Conclusions

In this work, a simultaneous topology and fibre orientation optimisation framework has been successfully developed and applied to optimised parts with isotropic and orthotropic material properties. The objective function for all optimisation cases was to minimise compliance with three distinct volume constraints: 30%, 40%, and 50% of an initial rectangular domain. Three classical benchmark cases are considered: cantilever beam, 3-point bending, and 4-point

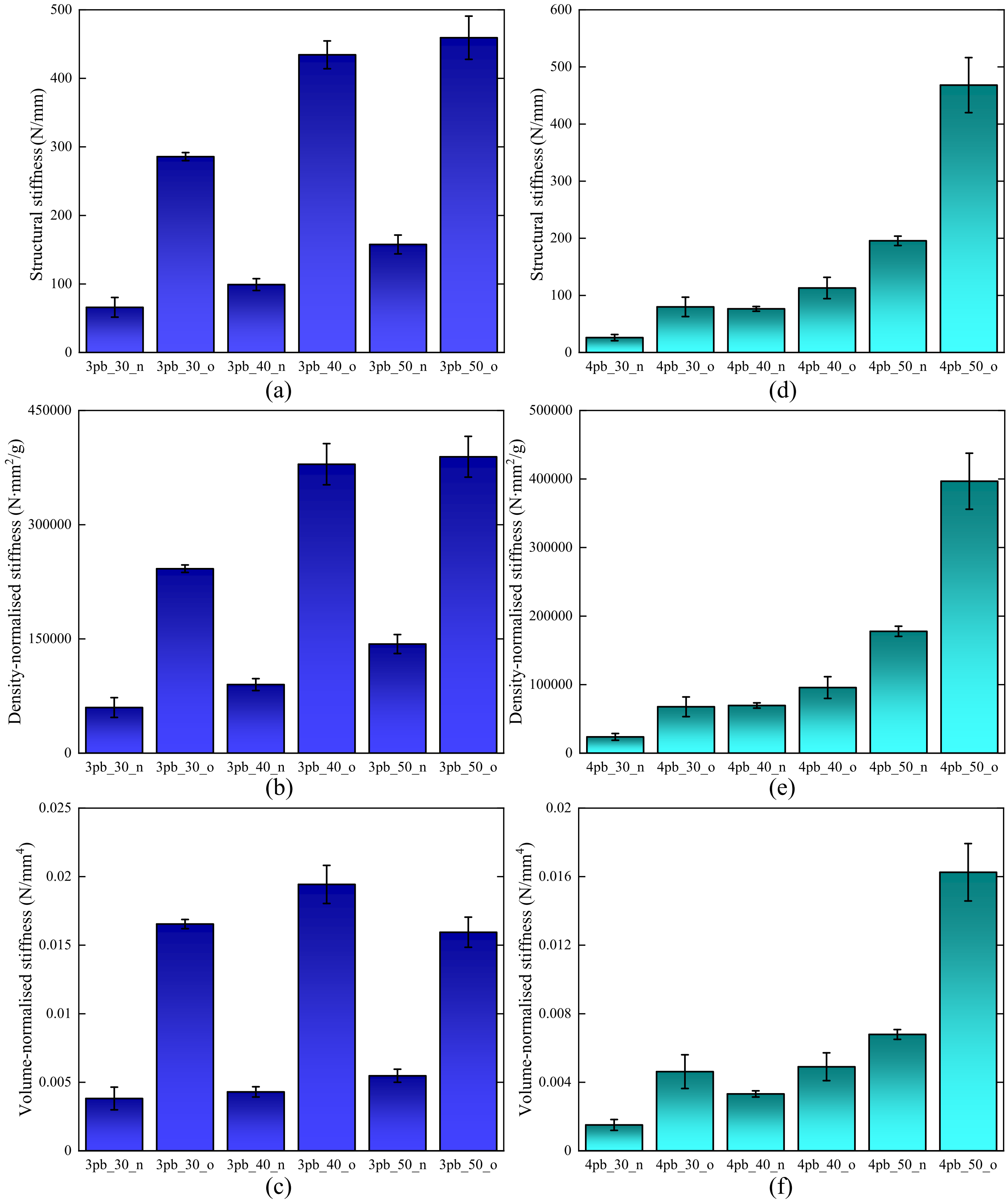

Figure 12: Structural stiffness for specimens under (a) 3-point and (b) 4-point bending. Density-normalised stiffness for (c) 3-point and (d) 4-point bending tests. Volume-normalised stiffness for samples under (e) 3-point and (f) 4-point bending.

bending. The optimised parts under 3-point and 4-point bending were 3D printed using FFF technique and tested to validate the proposed framework. Samples optimised for the cantilever beam loading case were not considered in the experimental campaign because the boundary conditions used in the optimisations could not be reproduced experimentally with the equipment available.

The proposed framework was extremely effective at maximising the structural stiffness for both nylon (isotropic) and onyx (orthotropic) parts. Experimental results showed that the density- and volume-normalised stiffnesses of onyx parts were significantly stiffer than those of nylon samples, which indicates that the concurrent framework was extremely efficient to optimise the chopped CFRP composite parts at different admissible volumes. This framework can play a key role in saving weight for additively manufactured CFRP structures. In the future, we plan to extend this framework to minimise weight under design load constraints.

Acknowledgements

HA is supported by the Royal Academy of Engineering under the Research Fellowship scheme [Grant No. RF/201920/19/150]. VT acknowledges CNPq (process No. 310656/2018-4) and CAPES-FCT (No. AUXPE 88881.467834/2019-01 - Finance Code 001).

References

[1] O. Sigmund, K. Maute, Topology optimization approaches, Structural and Multidisciplinary Optimization 48 (2013) 1031—-1055. doi:10.1007/s00158-013-0978-6.

[2] M. P. Bendsøe, N. Kikuchi, Generating optimal topologies in structural design using a homogenization method, Computer Methods in Applied Mechanics and Engineering 71 (2) (1988) 197 – 224. doi:10.1016/0045-7825(88)90086-2.

[3] M. P. Bendsøe, Optimal shape design as a material distribution problem, Structural Optimization 1 (1989) 192 – 202. doi:10.1007/BF01650949.

[4] G. I. N. Rozvany, M. Zhou, T. Birker, Generalized shape optimization without homogenization, Structural Optimization 4 (1992) 250–252. doi:10.1007/BF01742754.

[5] B. Bendsøe, O. Sigmund, Material interpolation schemes in topology optimization, Archive of Applied Mechanics 69 (1999) 635–654. doi:10.1007/s004190050248.

[6] B. G. Christoff, H. Brito-Santana, E. L. Cardoso, J. L. Abot, V. Tita, A topology optimization approach used to assess the effect of the matrix impregnation on the effective elastic properties of a unidirectional carbon nanotube bundle composite, Materials Today: Proceedings 8 (2019) 789–803, 4th Brazilian Conference on Composite Materials (BCCM4), July 22-25th 2018. doi:https://doi.org/10.1016/j.matpr.2019.02.021.

[7] J. H. S. Almeida Jr., L. Bittrich, T. Nomura, A. Spickenheuer, Cross-section optimization of topologically-optimized variable-axial anisotropic composite structures, Composite Structures 225 (2019) 111150. doi:https://doi.org/10.1016/j.compstruct.2019.111150.

[8] M. Y. Wang, X. Wang, D. Guo, A level set method for structural topology optimization, Computer Methods in Applied Mechanics and Engineering 192 (2003) 227–246. doi:10.1016/S0045-7825(02)00559-5.

[9] Y. M. Xie, G. P. Steven, A simple evolutionary procedure for structural optimization, Computer and Structures 49 (1993) 885–896. doi:10.1016/0045-7949(93)90035-C.

[10] X. Guo, W. Zhang, J. Zhang, J. Yuan, Explicit structural topology optimization based on moving morphable components (mmc) with curved skeletons, Computer Methods in Applied Mechanics and Engineering 310 (2016) 711–748. doi:10.1016/j.cma.2016.07.018.

[11] O. Sigmund, A 99 line topology optimization code written in matlab, Structural and Multidisciplinary Optimization 21 (2001) 120—127. doi:10.1007/s001580050176.

[12] J. H. S. Almeida Jr., L. Bittrich, A. Spickenheuer, Improving the open-hole tension characteristics with variable-axial composite laminates: Optimization, progressive damage modeling and experimental observations, Composites Science and Technology 185 (2020) 107889. doi:10.1016/j.compscitech.2019.107889.

[13] B. Brenken, E. Barocio, A. Favaloro, V. Kunc, R. B. Pipes, Fused filament fabrication of fiber-reinforced polymers: A review, Additive Manufacturing 21 (2018) 1 – 16. doi:10.1016/j.addma.2018.01.002.

[14] H. Mei, Z. Ali, Y. Yan, I. Ali, L. Cheng, Influence of mixed isotropic fiber angles and hot press on the mechanical properties of 3d printed composites, Additive Manufacturing 27 (2019) 150 – 158. doi:10.1016/j.addma.2019.03.008.

[15] S. Garzon-Hernandez, D. Garcia-Gonzalez, A. Jérusalem, A. Arias, Design of fdm 3d printed polymers: An experimental-modelling methodology for the prediction of mechanical properties, Materials Design 188 (2020) 108414. doi:10.1016/j.matdes.2019.108414.

[16] A. N. Dickson, J. N. Barry, K. A. McDonnell, D. P. Dowling, Fabrication of continuous carbon, glass and kevlar fibre reinforced polymer composites using additive manufacturing, Additive Manufacturing 16 (2017) 146 – 152. doi:10.1016/j.addma.2017.06.004.

[17] Q. He, H. Wang, K. Fu, L. Ye, 3d printed continuous cf/pa6 composites: Effect of microscopic voids on mechanical performance, Composites Science and Technology 191 (2020) 108077. doi:https://doi.org/10.1016/j.compscitech.2020.108077.

[18] S. Sanei, D. Popescu, 3d-printed carbon fiber reinforced polymer composites: A systematic review, Journal of Composites Science 4 (3) (2020) 98. doi:10.1016/j.matdes.2019.108414.

[19] F. Ning, W. Cong, J. Qiu, J. Wei, S. Wang, Additive manufacturing of carbon fiber reinforced thermoplastic composites using fused deposition modeling, Composites Part B: Engineering 80 (2015) 369 – 378. doi:10.1016/j.compositesb.2015.06.013.

[20] Y. Chen, L. Ye, Topological design for 3D-printing of carbon fibre reinforced composite structural parts, Composites Science and Technology 204 (2021) 108644. doi:10.1016/J.COMPSCITECH.2020.108644.

[21] Y. Chen, L. Ye, Designing and tailoring effective elastic modulus and negative Poisson's ratio with continuous carbon fibres using 3D printing, Composites Part A: Applied Science and Manufacturing 150 (2021) 106625. doi:10.1016/J.COMPOSITESA.2021.106625.

[22] K. Sugiyama, R. Matsuzaki, A. V. Malakhov, A. N. Polilov, M. Ueda, A. Todoroki, Y. Hirano, 3D printing of optimized composites with variable fiber volume fraction and stiffness using continuous fiber, Composites Science and Technology 186 (2020) 107905. doi:10.1016/j.compscitech.2019.107905.
URL https://doi.org/10.1016/j.compscitech.2019.107905

[23] M. Petrovic, T. Nomura, T. Yamada, K. Izui, S. Nishiwaki, Orthotropic material orientation optimization method in composite laminates, Structural and Multidisciplinary Optimization 57 (2) (2018) 815—828. doi:10.1007/s001580050176.

[24] J. Lee, D. Kim, T. Nomura, E. M. Dede, J. Yoo, Topology optimization for continuous and discrete orientation design of functionally graded fiber-reinforced composite structures, Composite Structures 201 (2018) 217 – 233. doi:10.1016/j.compstruct.2018.06.020.

[25] X. Tong, W. Ge, X. Gao, Y. Li, Optimization of combining fiber orientation and topology for constant-stiffness composite laminated plates, Journal of Optimization Theory and Applications 181 (2019) 653—-670. doi:10.1007/s10957-018-1433-z.

[26] D. Jiang, R. Hoglund, D. Smith, Continuous fiber angle topology optimization for polymer composite deposition additive manufacturing applications, Fibers 7 (2019) 14. doi:10.3390/fib7020014.

[27] T. Nomura, A. Kawamoto, T. Kondoh, E. M. Dede, J. Lee, Y. Song, N. Kikuchi, Inverse design of structure and fiber orientation by means of topology optimization with tensor field variables, Composites Part B: Engineering 176 (2019) 107187. doi:10.1016/j.compositesb.2019.107187.

[28] V. S. Papapetrou, C. Patel, A. Y. Tamijani, Stiffness-based optimization framework for the topology and fiber paths of continuous fiber composites, Composites Part B: Engineering 183 (2020) 107681. doi:10.1016/j.compositesb.2019.107681.

[29] X. Yan, Q. Xu, H. Hua, D. Huang, X. Huang, Concurrent topology optimization of structures and orientation of anisotropic ma-

terials, Engineering Optimization 52 (9) (2020) 1598–1611. doi:10.1080/0305215X.2019.1663186.

[30] M. P. Bendsoe, O. Sigmund, Topology optimization: theory, methods, and applications, Springer Science & Business Media, 2003.

[31] O. Sigmund, Morphology-based black and white filters for topology optimization, Structural and Multidisciplinary Optimization 33 (4) (2007) 401–424.

[32] J. Bezanson, A. Edelman, S. Karpinski, V. B. Shah, Julia: A fresh approach to numerical computing, SIAM review 59 (1) (2017) 65–98.

[33] C. Geuzaine, J.-F. Remacle, Gmsh: A 3-d finite element mesh generator with built-in pre-and post-processing facilities, International journal for numerical methods in engineering 79 (11) (2009) 1309–1331.

[34] T. J. Hughes, The finite element method: linear static and dynamic finite element analysis, Courier Corporation, 2012.

[35] J. Halpin, J. Kardos, The halpin-tsai equations: a review, Polymer Engineering and Science 16 (1976) 344 – 352. doi:10.1002/pen.760160512.

[36] T. Grimm, User's guide to rapid prototyping, Society of Manufacturing Engineers, 2004.

[37] P. Cignoni, M. Callieri, M. Corsini, M. Dellepiane, F. Ganovelli, G. Ranzuglia, et al., Meshlab: an open-source mesh processing tool., in: Eurographics Italian chapter conference, Vol. 2008, Salerno, Italy, 2008, pp. 129–136.

[38] C. K. Chua, K. F. Leong, C. S. Lim, Rapid prototyping: principles and applications, World Scientific Publishing Company, 2010.

[39] B. O. Community, Blender - a 3D modelling and rendering package, Blender Foundation, Stichting Blender Foundation, Amsterdam (2018).
URL http://www.blender.org

[40] O. Sorkine, Laplacian mesh processing, Eurographics (State of the Art Reports) 4 (2005).

[41] © 2020 Markforged Inc., Eiger (2020).
URL https://www.eiger.io/signin

A. Input data for the optimisations

This section briefly describes the required input data to perform all optimisation cases. Figure 13 shows the dimensional parameters and the number of elements used in the analyses. Figure 14 depicts the material properties for both Onyx and Nylon materials.

Figure 15 describes all parameters used in the optimisation procedure, including the TO parameters as well as filtering and moving limits parameters.

The boundary conditions are applied directly to the global arrays of the problem.

```
function Domain_data()

    #
    # Input - dimensions and mesh
    #
    # L - length
    # h - height
    # nL - number of elements - length
    # nh - number of elements - height
    # nelem - total number of elements
    #
    const L = 60.0
    const h = 30.0
    const nL = 180
    const nh = 90
    const nelem = nL*nh

    return L, h, nL, nh, nelem

end #function
```

Figure 13: Domain and FE mesh data.

```
function Material_data()
    #
    # onix
    # E1_o - Elasticity Modulus - Fibre direction
    # E2_o - Elasticity Modulus - transversal
    #                    to fibre direction
    # nu12_o - Poisson ratio
    # G12_o - Shear Modulus
    #
    # nylon
    # E_n - Elasticity Modulus
    # nu_n - Poisson ratio
    #
    const E1_o = 1.26E3
    const E2_o = 0.33E3
    const nu12_o = 0.39
    const G12_o = 0.37E3
    const E_n = 0.98E3
    const nu_n = 0.420

    # Into a single aray
    const props_o = [E1_o, E2_o, nu12_o, G12_o]
    const props_n = [E_n, nu_n]

    return props_o, props_n

end #function
```

Figure 14: Material properties.

```
function Optimization_data()
    #
    # Input - Optimization
    #
    # simp - penalization factor
    # eta - relaxation factor
    # step - allowed step
    # tol - tolerance for convergence
    # lambda1,lambda2 - initial bissection
    #                parameters for OC
    # frac - allowed volumetric fraction
    # N - allowed number of iterations
    #                (for each step)
    # Rmax - filtering radius
    # rho_min - minimum allowed density
    # rho_max - maximum allowed density
    # theta0 - initial value for the fiber angle
    # rho0 - initial value for the density
    #

    const simp = 3.0
    const eta = 0.5
    const step = 0.001
    const tol = 1E-12
    const lambda1 = 0.0
    const lambda2 = 1E5
    const frac = 0.3
    const N = 2000
    const Rmax = 0.5
    const rho_min = 0.001
    const rho_max = 1.0
    const theta0 = 0.0
    const rho0 = frac
    #
    # Moving limits and convergency criteria
    #
    # deltainf - moving limit update percentage (lower)
    # deltasup - moving limit update percentage (upper)
    # LMinf_theta - Minimum allowed moving limit (Fibre angle)
    # LMsup_theta - Maximum allowed moving limit (Fibre angle)
    # LMinf_rho - Minimum allowed moving limit (density)
    # LMsup_rho - Maximum allowed moving limit (density)
    # stop - porcentage of design variables variation
    #         to assume convergency
    # stop_iter - subsequent steps to assume convergency
    #

    const deltainf = 0.7
    const deltasup = 1.2
    const LMinf_theta = 0.01
    const LMsup_theta = 0.2
    const LMinf_rho = 0.01
    const LMsup_rho = 0.1
    const stop = 0.01
    const stop_iter = 10

    return simp, eta, step, tol, lambda1, lambda2, frac, N,
    deltainf, deltasup, LMinf_theta, LMsup_theta, LMinf_rho,
    LMsup_rho, Rmax, nvmax, theta_inicial, rho_min, rho_max,
    stop, stop_iter

end #function
```

Figure 15: Optimisation data.